# Optimized Ni-assisted graphene transfer to GaAs surfaces: Morphological, structural, and chemical evolution of the 2D-3D interface

Carlos Macías, Antonella Cavanna, Ali Madouri, Solène Béchu, Stéphane Collin, Jean-Christophe Harmand, Andrea Cattoni, Amaury Delamarre

**Optimized Ni-assisted graphene transfer to GaAs surfaces: morphological, structural, and chemical evolution of the 2D-3D interface**

Carlos Macías[1,2], Antonella Cavanna[1], Ali Madouri[1], Solène Béchu[3], Stéphane Collin[1], Jean-Christophe Harmand[1], Andrea Cattoni[4] and Amaury Delamarre[1,*]

[1] *Centre de Nanosciences et de Nanotechnologies (C2N), CNRS, Université Paris-Saclay, 91120 Palaiseau, France.*

[2] *Institut Photovoltaïque d'Ile-de-France (IPVF), 91120 Palaiseau, France.*

[3] *Institut Lavoisier de Versailles (ILV), Université de Versailles Saint-Quentin-en-Yvelines, Université Paris-Saclay, CNRS, UMR 8180, 45 avenue des Etats-Unis, Versailles Cedex 78035, France.*

[4] *Dipartimento di Fisica, Politecnico di Milano, 20133 Milano, Italy.*

* *Corresponding author: amaury.delamarre@c2n.upsaclay.fr*

**Abstract**

Large surface transfer is a long-standing challenge for applications that require stacking 2D and 3D materials with only a limited number of combinations and techniques currently found in the literature. We report a systematic study of CVD graphene transfer to GaAs surfaces by mechanical exfoliation from Ge(110) substrates using highly stressed Ni layers. A uniform contact at the 2D-3D interface, achieved by aircushion pressing, enables a high yield of the transfer process to GaAs and other substrates exceeding 95% of the initial surface over cm-scales. Raman spectroscopy verifies that the crystalline quality of the transferred graphene is similar to that of the as-grown graphene, with its initially high compressive strain partially relaxed and no unintentional doping. After a two-step selective etching of the Ni layer in $H_2SO_4$ : Sodium-n nitrobenzene sulfonate : thiourea (Transene etchant TFG) and HCl, we studied the surface chemistry of the resulting graphene/GaAs surfaces by X-ray photoelectron spectroscopy (XPS). Undoped GaAs remains unoxidized during the transfer process with an increase of the As-As related peaks due to preferential Ga dissolution during the acid-based deoxidation and etching processes, whereas p-type GaAs in contact with graphene showed corrosion damage attributed to a galvanic process with graphene acting as the cathode. This work provides new insights on the potential and processing constraints of dry-transferred graphene/GaAs heterostructures.

## 1. Introduction

Metal-assisted transfer of two-dimensional materials is increasingly studied towards atomic-precision thickness-control in the 2D layers and recyclability of the mother substrate [1]–[4]. The use of these techniques has been mostly limited to inert target substrates such as $SiO_2$ or polymers due to the processing challenges inherent to air- or water-unstable substrates such as III-V materials. However, large area graphene/GaAs heterostructures are attracting an increasing attention due to novel applications such as high efficiency solar cells [5], [6], dual-function FETs [7] or epitaxial growth platforms, which could allow the fabrication of free-standing, stress-free III-V thin films with relaxed lattice mismatch constraints and potentially enable reusing the high-cost single-crystalline substrates [8], [9].

III-V surfaces incongruently decompose at the temperatures needed for graphene growth, and C is well-known to cause unintentional acceptor doping of III-V materials. Thus, good quality monolayer graphene cannot be grown directly on III-V materials and needs to be transferred from foreign substrates. However, the widely used wet-transfer of graphene grown on Cu foils by chemical vapor deposition (CVD) typically leads to uncontrollable introduction of poly-methyl methacrylate residues chemisorbed on the graphene

[10]–[13], wrinkling, and GaAs oxides formed at the interface [14], [15], which strongly deteriorate the electronic properties of the graphene [16] and impede a successful epitaxial growth [8], [14], [15]. Transfer-related residues additionally cause high unintentional doping levels in the graphene [17]. These techniques require complete etching of the initial substrate, which increases chemical waste and reduces cost-effectiveness.

Ni-assisted dry transfer potentially solves the limitations suffered by mature wet-transfer techniques [1], [2]. It was first proposed by Kim et. al. to transfer graphene layers grown on SiC to various substrates [2] and later employed in the first studies about remote epitaxy [8]. A detailed understanding of the impact of the process on the surface and interface chemical environment is nevertheless crucial to establish the links between processing and properties and currently unclear in the literature. Particularly, the selectivity of widely used Ni etchants is generally poor with GaAs and other III-V materials, therefore dry-transferred graphene/GaAs heterostructures have been rarely reported in the literature. Moreover, the manual attachment of the exfoliated graphene/Ni stack to the target substrate usually leaves air bubbles and moisture trapped at the interface, which often provoke a partial failure of the transfer and severely affect the reliability of the process.

An adequate transfer adapted to the specific target substrate therefore sets the base for revealing novel physics and potential applications of mixed-dimensional systems. We report a highly reproducible approach to dry-transfer CVD graphene grown on Ge(110) using stressed Ni carrier layers, optimized for GaAs target substrates, and provide a thorough characterization of the fabricated heterostructures using Raman spectroscopy, optical and scanning electron microscopy (SEM) and X-ray photoelectron spectroscopy (XPS). Raman spectroscopy confirms a damage-free transfer well exceeding a 95% of surface yield while microscopic analyses and XPS show a residue and wrinkle-free surface across large surfaces with high spatial homogeneity. The transferred graphene has near-intrinsic levels of strain and doping and a low level of interface oxidation.

Remarkably, the use of Ge(110) as the growth substrate enables a four-fold reduction of the Ni stressor with respect to SiC due to the lower adhesion of graphene. It also significantly reduces the thermal budget of the process since SiC requires temperatures over 1300°C for graphene growth by thermal decomposition. Besides, while graphene growth on SiC and Cu surfaces intrinsically result in partially multilayer graphene, carbon insolubility and catalytic deposition on high quality Ge single crystals ensure a self-limited single layer graphene growth under optimized conditions [18].

## 2. Experimental

### *2.1. Graphene growth and transfer*

Figure 1 shows a schematic representation of the process workflow for graphene transfer. We grow single layer graphene on undoped epi-ready Ge(110) wafers (University wafers) by CVD using 3 sccm of $CH_4$ as the C precursor and 200 sccm of $H_2$ as the carrier gas in an Aixtron BM vertical showerhead reactor. At the growth temperature, $CH_4$ is decomposed on the Ge catalyst surface and forms the graphene. The wafers were introduced in the reactor after dipping in deionized water to dissolve the $GeO_2$ native oxide and annealed under $H_2$ for 900s at 910°C. We then turn on the $CH_4$ flow to obtain a full monolayer coverage in 1 hour, with a fixed pressure of 15 mBar inside the reactor. This results in full-coverage graphene with atomic-scale surface roughness (1.1 nm RMS) dictated by the step-terrace morphology of the underlying Ge, as shown in supplementary Fig. 1. More details about the growth can be found elsewhere [18], [19].

To transfer the grown graphene, we use a highly stressed Ni film deposited by e-beam evaporation at room temperature and a base pressure of 7 x $10^{-8}$ mBar. We keep the deposition rate below 3 Å/s to avoid damaging the graphene layer. The film thickness is calibrated by Stoney's approach (see Supplementary Materials) to obtain a stored elastic energy close to ~90% of the reported Ge(110)-graphene work of adhesion [20]. Prior to the transfer, we dip the p-type or semi-insulating (SI) GaAs wafers ((100) surface planes, AXT) in concentrated HCl to remove the native oxides and rinse in successive baths of isopropyl alcohol until reaching a pH~6.5-7.0. The graphene stack is later attached to a thermal release tape (TRT) (Nitto Revalpha 3400MS) and transferred to the GaAs target substrate by hot-pressing or aircushion pressing (Nanonex NX2500) at 90°C and an applied pressure of 0.69-3.45 MPa. We assess the pressure uniformity with a surface profiler film (SPF-C) that provides a quantitative measurement of the applied pressure within 10% of relative accuracy. After lifting-off the TRT on a hot-plate at 130°C we clean the organic residues left on the GaAs/graphene/Ni using an $SF_6/O_2$ plasma (10 sccm/2 sccm, 10W) and chemically etch the Ni layer with successive baths in $H_2SO_4$ : sodium n-nitrobenzenesulfonate : thiourea in $H_2O$ (Transene etchant TFG) and $HCl_{(aq)}$ (37%). The samples were finally rinsed in running deionized water and dried with $N_2$. For some experiments (see Fig. 2), $Si/SiO_2$ (90 nm) was used as the target substrate to facilitate the identification of graphene and the quantification of the transfer yield by optical microscopy. $FeCl_{3(aq)}$ (30%) was used to etch the Ni layer on graphene/$SiO_2$.

*2.2. Characterization*

We use Raman spectroscopy to ascertain the graphene transfer and assess the structural quality using a Renishaw InVia confocal µ-Raman setup with a 532 nm laser excitation source, a 1800 l/mm diffraction grating and a 100x objective (NA=0.85). The setup is operated with an excitation power of 0.72 mW to minimize laser induced heating.

SEM images were taken with a Magellan 400L equipped with a through-the-lens secondary electron detector and operated at 2 kV to maximize surface contrast sensitivity and reveal contaminants and topographic details which are invisible with a conventional Everhart-Thornley detector, while minimizing charging effects. Surface yield of the transfer process was quantified thresholding optical and SEM images with the ImageJ software [21].

For XPS measurements, we use a Thermo Scientific K-Alpha photoelectron spectrometer with a monochromatic Al $K_\alpha$ source (1486.6 eV), charge compensation on SI-GaAs substrates and a take-off angle of 90°. The Thermo Electron procedure was used to calibrate the Nexsa spectrometer by using metallic Cu and Au intern references (Cu $2p_{3/2}$ at 932.6 eV and Au $4f_{7/2}$ at 84.0 eV). High energy resolution spectra were acquired with an X-ray spot size of 400 µm and using a constant analyzer energy (CAE) mode of 20 eV and 0.1 eV as energy step size. Data were processed using the Thermo Fisher Scientific Avantage© software: for the non-linear least square decomposition, symmetrical Lorentzian-Gaussian mixes (30%) were used, except for the C 1s graphene photopeak, simulated with an asymmetrical tail mix of 61%. XPS spectra were treated using a Shirley background subtraction, and XPS compositions were deduced using the sensitivity factors and the inelastic mean free paths from Avantage library associated with the spectrometer and the corresponding transmission function. Following previous analysis of graphene and graphitic materials [22], [23] , beside the asymmetric C = C $sp^2$ component of the C 1s peak, we consider common O-containing functional groups and a "defect" peak at 285 eV; all represented by symmetrical Lorentzian-Gaussian functions. The later peak is associated with $sp^3$ bonds over the surface, non-conjugated C, and C-H bonding, generally termed as defects, and accounts for the slight broadening of the envelope observed after graphene transfer.

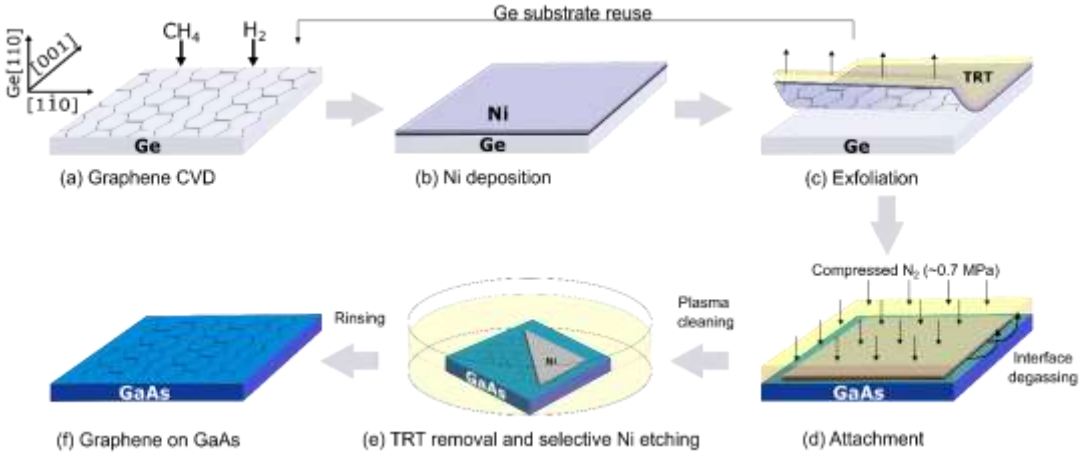


Figure 1: Schematic of the transfer process. a-c) The graphene is deposited on Ge (110) by CVD and exfoliated with Ni/TRT. d) The stack is attached to the GaAs substrate by aircushion pressing. e, f) After the removal of organic residues with an $O_2/SF_6$ reactive ion etching the Ni layer is removed by chemical etching.

## 3. Results and discussion

### *3.1. Dry transfer and structural quality*

A schematic illustration of our transfer process is shown in figure 1. First, an adequate release layer needs to be deposited on the graphene surface. To achieve a successful detachment of the graphene layer, the crack propagation path needs to be predefined at the graphene/Ge interface. In other words, the work of adhesion ($W_A$) between the graphene and the handling layer must be larger than that between graphene and the Ge substrate. For this reason, we choose Ni as the handling layer, which has the strongest adhesion to graphene among all the studied transition metals. Although reported values for $W_A^{Ni-graphene}$ vary by as much as an order of magnitude depending on the measurement or simulation approach (3.5 $Jm^{-2}$ – 72.7 $Jm^{-2}$) [24]–[26], as it is dependent on several factors such as the surface morphology, crystal face, stress state and delamination mode mixity, it is expected to be much stronger than $W_A^{graphene-Ge(110)}$, which is on the order of 0.158 $Jm^{-2}$ [20].

As previously found by Kim et al. [2] we observe a beneficial impact of using Ni films with a stored elastic energy close to the expected value of $W_A^{graphene-Ge(110)}$. Internal stress in the Ni layer imposes a shear stress at the graphene-Ge interface provoking mixed mode I and II crack propagation when the external bending moment is applied. This situation prevents the crack to bend upwards through the graphene layer significantly improving the uniformity of the transfer. Additionally, the stored elastic energy is partially released during the exfoliation minimizing the energy (peeling force) that needs to be applied externally. Details about the control of the stored elastic energy via the deposited thickness are given in Fig. S2 (Supplementary material). The process is optimized for a thickness of 100 nm of Ni which provides a stored elastic energy of ~93% of the graphene/Ge work of adhesion [20], while the optimum thickness depends on the resulting internal stress after Ni deposition. SEM images in Fig. S2 c show how thorns are easily formed when the exfoliation is carried out with a 50 nm Ni layer, with an insufficient stored strain energy. Only anisotropic cracks perpendicular to the peel-off direction with a period of one to several mm remain present

as a consequence of the tensile stress applied to the Ni during the exfoliation process, similar to what was shown in [1]. While intact graphene areas are wide enough for most applications (especially those that do not require long-distance lateral current transport in the graphene above GaAs, e.g. solar cells [5], [6] or epitaxy above the graphene [8], [9]), we propose that ultimate suppression of cracking requires a proper design of the mechanical properties in the polymeric film.

The exfoliated stack needs to be attached to the target substrate ensuring that no air bubbles and moisture remain trapped at the interface to achieve a sufficient adhesion that enables the TRT removal and further processing without lifting-off the graphene. We found that applying a controlled pressure is necessary to achieve an intimate contact between the graphene and the target substrate and enable high yields; otherwise, the graphene-substrate adhesion is not enough leading to failure during the release of the TRT. Moreover, pressure in a conventional parallel-plate wafer bonding press is very sensitive to thickness variations across the wafer, trapped particles and small misalignments that typically result in a highly uneven pressure and a subsequent partial failure of the transfer process with large un-transferred areas. Even the insertion of a PDMS stamp in between the stack of interest and the press did not lead to a sufficiently homogeneous applied pressure. Therefore, we applied aircushion pressing developed for nanoimprint technology [27] to properly outgas the interface under vacuum and achieve a high uniformity in applied pressure across large surfaces. Fig. 2 shows a comparison of pressure maps obtained by hot pressing and aircushion pressing and the resulting optical images of graphene transferred to $SiO_2$. While hot pressing (Fig. 2a, c, e) typically results in a weakly adhered graphene and low transfer yields (below 50% of the initial surface), aircushion pressing greatly improves pressure uniformity and increases the yield well above a 95% of the initial surface and the reproducibility of the process. The experimental P and T profiles are provided in Fig. S3 a. The optimum pressure was found to be ~0.7 MPa while higher pressures led to a significant degradation of the Raman figures of merit as shown in Fig. S3 b, possibly due to the Poisson's effect in the soft polymeric film. The process yields a smooth surface on graphene/$SiO_2$ (RMS roughness of 0.7 nm) as shown by AFM in Fig. S4 a.

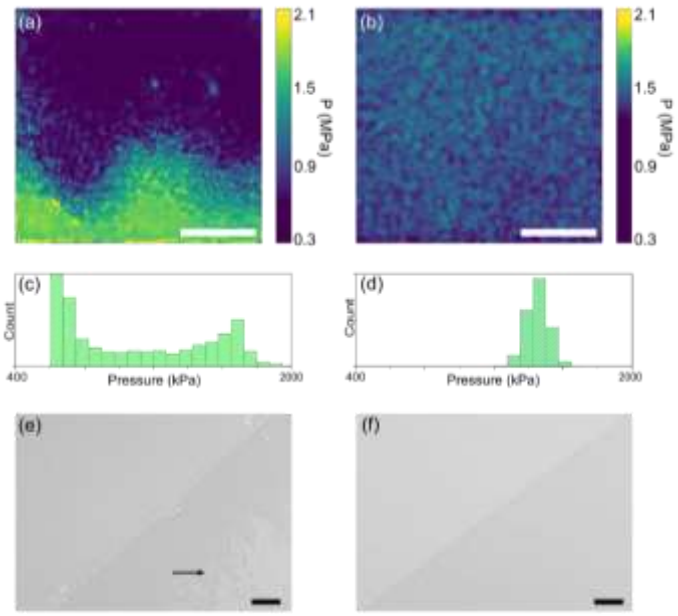


Figure 2: Effect of aircushion pressing. a, b) Pressure maps obtained by hot pressing and aircushion pressing, respectively. c, d) Pressure histograms extracted from the maps in a and b, respectively. In this demonstration, the nominal

pressure applied was 1400 kPa. e, f) Nomarski optical images of graphene transferred to $SiO_2$ using hot pressing and aircushion pressing respectively. The arrow in e highlights a damaged region. The scale bars are 3 mm in a, b and 200 µm in e, f.

We use Raman spectroscopy to verify the success of the transfer and evaluate the structural quality of the graphene. Fig. 3a shows the spatially averaged (400 measurement points) Raman spectrums of a typical sample before (on Ge(110)) and after transfer to GaAs. The three main bands of the graphene can be observed, namely the D band (~1350 $cm^{-1}$), the G band (~1600 $cm^{-1}$) and the 2D band (~2700 $cm^{-1}$) [28]. The appearance of the momentum conservation-forbidden D band indicates the presence of structural defects in the graphene layer. However, we note that D peak is equally intense in the as-grown sample, and therefore arising from non-optimized growth conditions. As the $I_D/I_G$ intensity ratio of the transferred sample ($I_D/I_G$≈0.16) does not increase significantly with respect to the as- grown sample ($(I_D/I_G)_0$≈0.14) we conclude that the transfer process is not introducing additional defects. In the low defect density regime, the surface density of Raman active point-like defects can be estimated as [29]:

$$n_d(\mathrm{cm}^{-2}) = 7.3 \times 10^9 E_L^4 \left({}^{I_D}/_{I_G}\right) \quad , \tag{1}$$

Where $E_L$ is the excitation source photon energy, which yields 3.3×$10^{10}$ $cm^{-2}$ in the transferred sample and 2.9×$10^{10}$ $cm^{-2}$ in the as-grown sample. Hyperspectral Raman maps of the double resonance 2D band and the $I_{2D}/I_G$ intensity ratio of the transferred sample are shown in Fig. 3a, b. The uniform presence of the 2D band over the measured area indicates continuity of the graphene layer. On the other hand, the $I_{2D}/I_G$ between 1 and 3 (Fig. 3b and Fig. 3c) proves that the graphene is monolayer and highly crystalline over the whole surface. Similar maps can be reproduced on different regions of the sample.

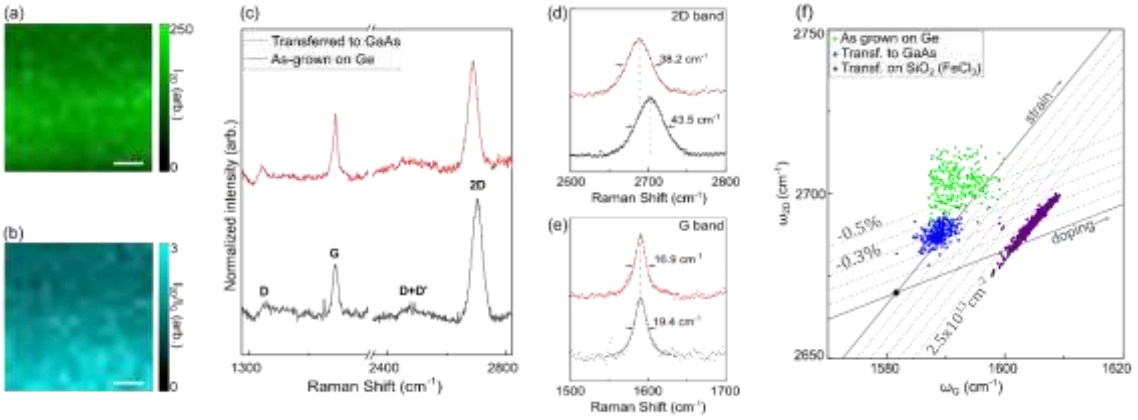


Figure 3: Raman characterization of graphene transferred to GaAs. a, b) Raman maps of the 2D band intensity (a) and the 2D/G intensity ratio (b) of the graphene transferred to GaAs. The scale bars are 3 µm long. c) Stacked Raman spectra of the transferred sample (red) compared to the as-grown sample (black). d, e) Magnified views of the 2D (d) and G (e) bands for the as-grown graphene (black) compared to the transferred graphene on GaAs (red). The solid curves correspond to Lorentzian fits of the experimental data. The values of the FWHM are shown next to each peak. Phonon softening after the transfer is evident specially on the 2D band due to stress relaxation. f) Correlation of the 2D-G peak positions with the strain and doping of the graphene on the growth substrate (green), dry-transferred to GaAs (blue) and dry-transferred to $SiO_2$ (purple).

We investigate the effect of the transfer on the strain and charge carrier density using the vector

decomposition correlation analysis of the G and 2D frequencies proposed by Lee et al. [30]. Both the strain and doping can be simultaneously estimated from the different 2D and G peak shifts expected. Biaxial strain displaces the peaks along a line that satisfies $\Delta\omega_{2D}/\Delta\omega_G \approx 2.2$ while p-type doping shifts follow $\Delta\omega_{2D}/\Delta\omega_G \approx 0.55$ from the neutral point $(\omega_G^0,\ \omega_{2D}^0)$=(1581.6, 2676.9) $cm^{-1}$ measured for freestanding monolayer graphene [30]. Fig. 3f shows the $\omega_{2D} - \omega_G$ scatter plot with superimposed strain and charge density axes. The initially wide data cloud dispersion arises from spatial point-to-point variations resulting from the graphene growth process on Ge. AFM imaging of the as-grown graphene (Fig. S1) suggests that wrinkles and deep step bunches appearing at distances comparable or larger than the laser spot size may be behind such non-uniformity. These morphological features appear to relieve compressive strain arising from the negative thermal expansion coefficient of graphene between the growth temperature and room temperature [31], and are expected to introduce spatial variations in both strain [32], [33] and charge carrier densities [34], [35]. The buildup of mixed biaxial and uniaxial strain components during this partial relaxation process can also deviate the dispersion from the assumed $\Delta\omega_{2D}/\Delta\omega_G \approx 2.2$, as detailed in [30]. A larger uncertainty in the determination of peak positions on Ge (±1.34 $cm^{-1}$) compared to $SiO_2$ (±0.07 $cm^{-1}$) due to a lower signal/noise ratio in the former can also contribute to the wider dispersions observed on Ge.

Clear trends can be obtained from Fig. 3f for the evolution of strain and doping when transferring the graphene to foreign substrates. We observe that the initially high biaxial compressive strain (between -0.5% and -0.7%), is partially released during the transfer (between -0.2% and -0.4%). Estimated carrier densities in graphene/GaAs remain very low (< 5 x $10^{12}$ $cm^{-2}$), indicating that neither the GaAs surface nor transfer-induced adsorbates behave as acceptors, which is desirable for transferred graphene as it opens the way to study intrinsic properties and to controllably dope it ex-situ. In contrast, dry transferred graphene on $O_2$-plasma treated $SiO_2$, where the Ni was etched by ferric chloride, shows a similar trend on the stress relaxation but a high p-type unintentional doping (> 2.5 x $10^{13}$ $cm^{-2}$). This is mainly attributed to substrate effects since our PMMA-assisted wet transfer process did not result in such a high doping (see Fig. S5 and supplementary note 3), i.e, undoped GaAs does not induce acceptor levels as in the case of $SiO_2$. We note that the iron (III) chloride etchant used to remove Ni on $SiO_2$ may also contribute to such a high doping, since hole doping by metal chlorides has been widely observed [36]–[38].

Other effects could cause different Raman peak dispersion relation between graphene on Ge, GaAs or $SiO_2$. For instance, the crystalline nature of the former two can lead to reconstruction effects and uniaxial strains. A detailed nanoscale study combining scanning tunneling microscopy and tip-enhanced Raman spectroscopy would allow a detailed understanding of these differences by correlating directly observable morphological, chemical and structural local inhomogeneities with their spatially resolved spectral fingerprint and is left for a future work.

### *3.2. Surface chemistry: selective etching and corrosion effects*

We now discuss the selective chemical etching of the Ni carrier layer and its effect on the graphene/GaAs surface. Widely used Ni etchants such as aqueous $FeCl_3$ and strongly oxidizing acid solutions are not compatible with GaAs. Other non-oxidizing strong acids such as HCl or $H_2SO_4$ can provoke a strong damage to the graphene due to $H_2$ bubbling produced by the reaction with the Ni film, as shown in Fig. S6. The use of an acid solution containing a stronger electron acceptor is therefore desirable to dissolve the Ni layer without bubbling. We use an aqueous acid solution containing nominally 10%–15% Sodium n-nitrobenzene

sulfonate as the oxidizer, 1% Thiourea as a complexing agent and less than 10% sulfuric acid (Transene TFG), which provides a high selectivity etching (> 20:1) of Ni on GaAs.

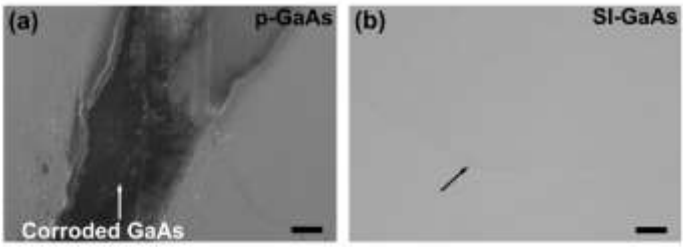


Figure 4: Corrosion damage in GaAs. a) Nomarski optical micrograph of graphene transferred to p-type GaAs where corrosion damage is evident on the exposed region. b) Nomarski optical micrograph of graphene transferred to SI-GaAs without corrosion damage. The graphene edge is weakly visible at the position of the arrow. The scale bars are 50 μm.

However, we found that p type-doped GaAs may suffer a strong corrosion damage when the graphene is present at the Ni/GaAs interface, accelerated on graphene openings as shown in Fig. 4a. It is known that GaAs in contact with noble metals is prone to suffering galvanic corrosion in acid media [39], [40]. On the other hand, it has been reported that directly grown graphene enhances room-temperature corrosion of Cu due to galvanic coupling [41], and graphite is known to cause galvanic corrosion of various metals and semiconductors including Si [42]. Therefore, we attribute the observed behavior to a galvanic process with graphene acting as the cathode. Anodic dissolution of GaAs may occur through the following oxidation partial reactions at pH 0:

$$GaAs_{(s)} + 2H_2O + 6h^+ \rightarrow Ga^{3+} + HAsO_{2(aq)} + 3H^+$$

$$GaAs_{(s)} + 4H_2O + 8h^+ \rightarrow Ga^{3+} + H_3AsO_{4(aq)} + 5H^+$$

And the dissolution rate is generally dominated by the capturing of holes by surface bonds in the absence of other limiting steps [43]. Illumination with sufficiently low wavelengths increases the dissolution rate due to an increase of charge carrier densities close to the surface. In any case, corrosion also occurs at lower rates when the etching is performed in the darkness (Fig. S7). For p-type GaAs in darkness, electron densities in the conduction band are low, hence electron transfer is mostly limited to a valence band process. This suggests that the electron (hole) transfer to the cathode (anode) can be mediated solely by the GaAs valence band despite the relatively large barrier for hole injection from the graphene predicted by the Schottky-Mott rule (~0.89 eV for $[Zn_{Ga}]=10^{19}$ $cm^{-3}$). On the other hand, as Fig. 4b shows, corrosion is suppressed on SI-GaAs possibly due to the decrease in charge carrier concentration. A careful design of the etching solution and the doping level in GaAs would be needed to extend the applicability of this method to p-GaAs.

After an etching step in TFG solution, most of the Ni is dissolved leading to an optically clean surface as shown in Fig. 4b. We use XPS to investigate the chemical state of the fabricated graphene/GaAs heterostructures and verify the absence of contaminants. XPS surveys in Fig. 5a revealed the presence of Ni residues that could be sometimes observed by SEM inspection as seen in Fig. 5c. A significant attenuation of the Ga and As peaks in Fig. 5a (green curve) is also a consequence of surface contaminants on the graphene.

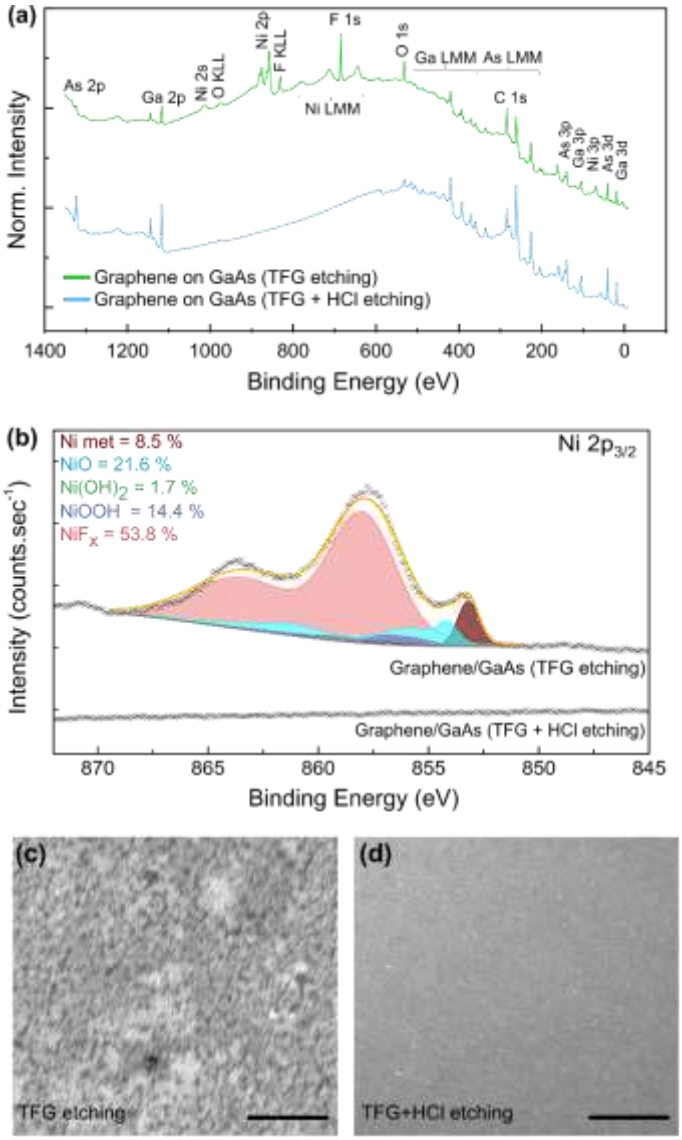


Figure 5: Removal of Ni residues. a) XPS surveys after a first etching step in TFG (green curve) and after the second step in HCl (blue curve). b) High resolution XPS spectra of Ni 2p and F 1s peaks before etching with HCl. c, d) SEM images of graphene transferred to GaAs before and after a second etching step with HCl. The scale bars are 10 µm.

Figure 5b shows the high-resolution spectra of Ni 2p. The weak first feature of the Ni $2p_{3/2}$ multiplet at a binding energy of 853.5 eV suggests a mix between metallic Ni and oxidized forms (NiO and NiOOH) [44], [45]. The second Ni $2p_{3/2}$ photopeak appearing at 858.0 eV together with the F 1s line at 685.0 eV indicates the formation of $NiF_x$ (B.E.(Ni $2p_{3/2}$)=857.4 – 858.2 eV) as the major contribution, consequence of the $SF_6/O_2$ plasma cleaning used to remove the remaining organic residues from the TRT prior to the wet etching. The quantitative analysis of the XPS results is presented in table S1. Fits of the Ni $2p_{3/2}$ in Fig. 5b confirm these observations. Other oxidized forms of Ni such as oxyhydroxides and hydroxides are also present and overlapped with the previously discussed species. These results show that the naturally formed NiO passivation layer is further grown by the action of the plasma together with the formation of $NiF_x$. In many iterations it was found that these residues cannot be dissolved by TFG etching alone, even for etching times exceeding 2h. On the exposed GaAs surface, the plasma forms a passivating $GaAsO_xF_y$ layer [46]. We also note that chemical dissolution of the TRT residues by organic solvents is not possible due to spontaneous delamination of the Ni/graphene layer. Due to the low interface energies between graphene and non-polar

solvents like acetone or toluene, the effective work of adhesion between graphene and the substrate is sharply reduced when the sample is dipped in the solvent, which, together with the residual stress in the Ni layer, makes spontaneous lift-off energetically favorable. Contact angle measurements of different liquids on the surfaces in contact (freshly deoxidized GaAs and graphene on Ni) are consistent with this observation and predict a spontaneous $W_A$ lowering of ~35 mJ/m$^2$ upon immersion of the sample in acetone (Fig. S8).

To remove the remaining Ni-containing residues we introduce a second etching step using HCl (37%). One can see in the XPS survey of Fig 5a (blue curve) that the Ni and F photoemission lines are no longer present. Also, the SEM image of Fig 5d shows a uniform surface with no evidence of contamination. We therefore conclude that a two-step chemical etching in TFG and concentrated HCl successfully eliminates the Ni carrier layer. A relatively smooth, mirror-like surface is recovered, showing an RMS roughness of 2.1 nm as measured by AFM in Fig. S4.

At this stage, we could verify monolayer thickness of the graphene comparing the integrated intensity of the main component in the C1s photopeak to that of a reference monolayer sample on GaAs (wet transferred, Fig. S9). At an emission angle $\alpha$ (w.r.t. the surface normal), the intensity of electrons at the analyzer photoemitted from a continuum medium with an effective attenuation length $\lambda$ can be calculated integrating the photoemission intensity in-depth (i.e. $I(z) = I_0 \exp(-z/\lambda \cos\alpha)$). The quotient between the total measured intensity and the reference monolayer intensity can thus be written as:

$$\frac{I_m}{I_{SLG}} = \frac{[1-e^{-t_m/\lambda \cos\alpha}]}{[1-e^{-t_{SLG}/\lambda \cos\alpha}]} \quad ; \tag{2}$$

where $t_m$ is the measured graphene thickness and $t_{SLG}$ is the reference monolayer thickness (0.336 nm). Solving $t_m$ yields an estimation of ~0.8 ML of graphene, in agreement with Raman spectra; a value lower than nominally one monolayer is a consequence of multilayer patches in the reference wet transferred sample grown on Cu.

Let us now focus on the effect of the transfer process on the chemical environment of the GaAs surface and the graphene layer. Fitted XPS As, Ga and C peaks are presented in figure 6. Both the 3d (Fig 6a, b) and 2p$_{3/2}$ (Fig 6d, e) peaks of Ga and As provide complementary information due to the different probing depth. Low kinetic energy electrons from the 2p levels provide more surface sensitiveness due to the reduced effective attenuation length. The information depth can be estimated as:

$$S_p = \lambda(E_k) \cos\alpha \ln\left[\frac{1}{1-(P/100)}\right] \quad , \tag{3}$$

Where $P$ is the percentage of the signal generated within a distance equal to $S_p$ from the surface. Using the inelastic mean free paths for GaAs calculated by Shinotsuka et al. [47] and the single scattering albedo tabulated by Jablonski and Powell [48] to estimate $\lambda(E_k)$, Eq. 3 yields 1.6 nm and 2.7 nm for As and Ga 2p$_{3/2}$ electrons respectively, and 7.6 nm and 7.7 nm for As and Ga 3d electrons respectively ($P = 99\%$ of the signal).

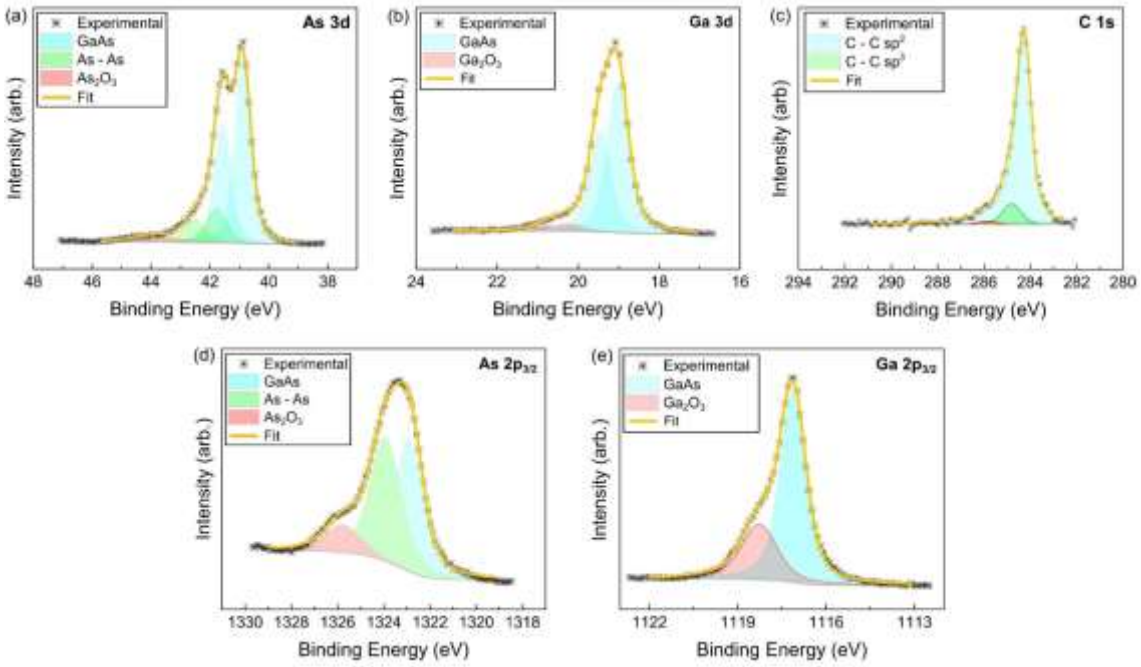


Figure 6: Curves to fitted XPS data (Ga, As and C photopeaks of a transferred sample). a, d) As 3d and $2p_{3/2}$ peaks, respectively. b, e) Ga 3d and $2p_{3/2}$ peaks respectively. c) C 1s peak.

Ga and As peaks in Fig.6 show a remarkably low level of oxidation at the GaAs/graphene interface compared to graphene transferred to GaAs by the wet route (fig. S9). The main chemical environment is related to GaAs (B.E. GaAs = 1117.1 ± 0.2 eV and B.E. = 19.0 ± 0.2 eV for Ga $2p_{3/2}$ and Ga $3d_{5/2}$ photopeaks, respectively, and B.E. GaAs = 1322.9 ± 0.2 eV and B.E. = 40.9 ± 0.2 eV for As $2p_{3/2}$ and As $3d_{5/2}$ peaks).The oxide, mainly composed by a mixture of $Ga_2O_3$ (Ga $2p_{3/2}$ oxide component at 1118.3 ± 0.2 eV and Ga $3d_{5/2}$ oxide component at 20.3 ± 0.2 eV) and $As_2O_3$ (As $2p_{3/2}$ oxide component at 1325.8 ± 0.2 eV and As $3d_{5/2}$ oxide component at 43.6 ± 0.2 eV), is contained within the first nm from the surface. The measured atomic percentages of $Ga_2O_3$ and $As_2O_3$ in this region are as low as 4.3% and 1.8% respectively and fall down to 1.3% and ~0 % when estimated from the 3d levels (see table S1). On the other hand, a slight As enrichment is evident in both 2p and 3d peaks with elemental As (As $2p_{3/2}$ elemental component at 1322.8 ± 0.2 eV and As $3d_{5/2}$ elemental component at 41.5 ± 0.12 eV) concentrations of 7.3% and 5.6%, and overall Ga/As ratios of 0.97 and 0.72 respectively. This is a consequence of the GaAs deoxidation in concentrated HCl prior to the graphene transfer, well known to form a metallic As capping layer [49]. As enrichment may further progress during the etching steps in acid solutions if reactions take place through graphene defects [50]. We note that As and $As_2O_3$ can be thermally desorbed at relatively low temperatures compared to $Ga_2O_3$. Further investigation on the removal of the As-rich layer is out of the scope of the present work but would be desirable for certain device applications, as $As_{Ga}$ antisite defects are well known deep levels in GaAs [51]. Overall, the composition of the GaAs lying under the graphene is very similar to that of a freshly HCl-deoxidized sample [52].

C 1s peak is shown in Fig. 6 c. A slight widening of the peak was observed in the transferred sample (FWHM=0.89±0.03 eV) compared to the as-grown sample (FWHM=0.70±0.03 eV). We added a second component to account for a possible increase in the $sp^3$ bonding character of the graphene layer

(hydrogenated and out-of-plane C atoms, BE=285.0 eV) and adventitious carbon. The FWHM of the asymmetric curve accounting for the metal-like $sp^2$ carbon contribution was constrained to ±0.05 eV of the FWHM measured on the freshly grown sample. Additionally, oxygenated functional groups common in graphitic materials were considered: hydroxyl (C–OH, 285.7 eV), epoxy (C–O–C, 286.7 eV), carbonyl (C=O, 288.0 eV) and carboxyl (O–C=O, 289.1 eV), and found to have negligible contributions to the C 1s line shape, in contrast with wet transferred graphene samples (Supplementary note 3).

## Conclusions

In conclusion, dry-transfer of CVD graphene grown on Ge(110) using stressed Ni layers and aircushion pressing is a promising technique to obtain high quality clean graphene on various substrates, significantly reducing processing time with respect to wet transfer routes and relevant to applications particularly if (i) growth substrate reuse is necessary (non-destructive for the mother wafer), (ii) the interface between graphene and the target substrate has specific surface preparations that need to be preserved during the transfer and (iii) if thin films deposited on the graphene need to be transferred as well (for example, for Van der Waals metal contacts). Raman spectroscopy and microscopic analysis verified the continuity of the transferred graphene/GaAs and the absence of structural damage during the transfer, as well as a release of thermal stresses imposed by the growth substrate and a reduced unintentional doping. Success of the transfer strongly depends on selectivity of process etchants that can be strongly affected by graphene-induced (photo)electrochemical effects that deserve further investigation. In this case, a two-step Ni etching based on TFG and HCl provides a high selectivity and a residue and oxide-free surface as proven by XPS analysis on semi-insulating GaAs, while fine adjustment of doping levels and redox couples is necessary for a general applicability of the method if the substrate is conductive and especially if it has p-type doping.

**Acknowledgements**

This project has been supported by the French Government in the frame of the program of investment for the future (Programme d'Investissement d'Avenir - ANR-IEED-002-01). The authors acknowledge the French Renatech network. We thank L. Leroy, D. Decanini and A. Durnez for technical support.

## References

[1] A. V. Zaretski *et al.*, “Metal-assisted exfoliation (MAE): Green, roll-to-roll compatible method for transferring graphene to flexible substrates,” *Nanotechnology*, vol. 26, no. 4, 2015.

[2] J. Kim *et al.*, “Layer-resolved graphene transfer via engineered strain layers,” *Science (80-. ).*, vol. 342, no. 6160, pp. 833–836, 2013.

[3] J. Shim *et al.*, “Controlled crack propagation for atomic precision handling of wafer-scale two-dimensional materials,” *Science (80-. ).*, vol. 362, no. 6415, pp. 665–670, 2018.

[4] J.-Y. Moon *et al.*, “Layer-engineered atomic-scale spalling of 2D van der Waals crystals,” *Matter*, vol. 5, no. 11, pp. 3935–3946, Nov. 2022.

[5] X. Yu *et al.*, “High Efficient Solar Cell Based on Heterostructure Constructed by Graphene and GaAs Quantum Wells,” *Adv. Sci.*, vol. 10, no. 2, pp. 1–8, 2023.

[6] X. Li *et al.*, “18.5% efficient graphene/GaAs van der Waals heterostructure solar cell,” *Nano Energy*, vol. 16, pp. 310–319, 2015.

[7] C.-C. Tang, M.-Y. Li, L. J. Li, C. C. Chi, and J.-C. Chen, “Graphene-GaAs/AlxGa1−xAs heterostructure dual-function field-effect transistor,” *Appl. Phys. Lett.*, vol. 101, no. 20, p. 202104, Nov. 2012.

[8] Y. Kim *et al.*, “Remote epitaxy through graphene enables two-dimensional material-based layer transfer,” *Nature*, vol. 544, no. 7650, pp. 340–343, 2017.

[9] S. H. Bae *et al.*, “Graphene-assisted spontaneous relaxation towards dislocation-free heteroepitaxy,” *Nat. Nanotechnol.*, vol. 15, no. 4, pp. 272–276, 2020.

[10] X. Yang and M. Yan, “Removing contaminants from transferred CVD graphene,” *Nano Res.*, vol. 13, no. 3, pp. 599–610, 2020.

[11] W. Choi *et al.*, “Effect of annealing in Ar/H2 environment on chemical vapor deposition-grown graphene transferred with poly (Methyl Methacrylate),” *IEEE Trans. Nanotechnol.*, vol. 14, no. 1, pp. 70–74, 2015.

[12] L. H. Karlsson *et al.*, “Graphene on graphene formation from PMMA residues during annealing,” *Vacuum*, vol. 137, pp. 191–194, 2017.

[13] B. Zhuang, S. Li, S. Li, and J. Yin, “Ways to eliminate PMMA residues on graphene —— superclean graphene,” *Carbon N. Y.*, vol. 173, pp. 609–636, 2021.

[14] H. Kim *et al.*, “Impact of 2D-3D Heterointerface on Remote Epitaxial Interaction through Graphene,” *ACS Nano*, vol. 15, no. 6, pp. 10587–10596, 2021.

[15] H. Kim *et al.*, “Role of transferred graphene on atomic interaction of GaAs for remote epitaxy,” *J. Appl. Phys.*, vol. 130, no. 17, 2021.

[16] A. Pirkle *et al.*, “The effect of chemical residues on the physical and electrical properties of chemical vapor deposited graphene transferred to SiO2,” *Appl. Phys. Lett.*, vol. 99, no. 12, pp. 2009–2012, 2011.

[17] Y. Song, W. Zou, Q. Lu, L. Lin, and Z. Liu, “Graphene Transfer: Paving the Road for Applications of Chemical Vapor Deposition Graphene,” *Small*, vol. 17, no. 48, p. 2007600, Dec. 2021.

[18] J. H. Lee *et al.*, “Wafer-scale growth of single-crystal monolayer graphene on reusable hydrogen-terminated germanium,” *Science (80-. ).*, vol. 344, no. 6181, pp. 286–289, 2014.

[19] J. Dai *et al.*, “How Graphene Islands Are Unidirectionally Aligned on the Ge(110) Surface,” *Nano Lett.*, vol. 16, no. 5, pp. 3160–3165, 2016.

[20] S. J. Yang, S. Choi, F. O. Odongo Ngome, K. J. Kim, S. Y. Choi, and C. J. Kim, “All-Dry Transfer of Graphene Film by van der Waals Interactions,” *Nano Lett.*, vol. 19, no. 6, pp. 3590–3596, 2019.

[21] C. A. Schneider, W. S. Rasband, and K. W. Eliceiri, “NIH Image to ImageJ: 25 years of image analysis,” *Nat. Methods*, vol. 9, no. 7, pp. 671–675, 2012.

[22] H. Estrade-Szwarckopf, “XPS photoemission in carbonaceous materials: A ‘defect’ peak beside the graphitic asymmetric peak,” *Carbon N. Y.*, vol. 42, no. 8–9, pp. 1713–1721, 2004.

[23] A. Kovtun, D. Jones, S. Dell, E. Treossi, A. Liscio, and V. Palermo, “Accurate chemical analysis of oxygenated graphene-based materials using X-ray photoelectron spectroscopy,” *Carbon N. Y.*, vol. 143, pp. 268–275, 2019.

[24] W. Chang, S. Rajan, B. Peng, C. Ren, M. Sutton, and C. Li, “Adhesion energy of as-grown graphene on nickel substrates via StereoDIC based blister experiments,” *Carbon N. Y.*, vol. 153, pp. 699–706, 2019.

[25] S. Das, D. Lahiri, D. Y. Lee, A. Agarwal, and W. Choi, “Measurements of the adhesion energy of graphene to metallic substrates,” *Carbon N. Y.*, vol. 59, pp. 121–129, 2013.

[26] J. Lahiri, T. S. Miller, A. J. Ross, L. Adamska, I. I. Oleynik, and M. Batzill, “Graphene growth and stability at nickel surfaces,” *New J. Phys.*, vol. 13, 2011.

[27] H. Gao, H. Tan, W. Zhang, K. Morton, and S. Y. Chou, “Air cushion press for excellent uniformity, high yield, and fast nanoimprint across a 100 mm field,” *Nano Lett.*, vol. 6, no. 11, pp. 2438–2441, 2006.

[28] A. C. Ferrari *et al.*, “Raman spectrum of graphene and graphene layers,” *Phys. Rev. Lett.*, vol. 97, no. 18, pp. 1–4, 2006.

[29] L. G. Cançado *et al.*, “Quantifying defects in graphene via Raman spectroscopy at different excitation energies,” *Nano Lett.*, vol. 11, no. 8, pp. 3190–3196, 2011.

[30] J. E. Lee, G. Ahn, J. Shim, Y. S. Lee, and S. Ryu, “Optical separation of mechanical strain from charge doping in graphene,” *Nat. Commun.*, vol. 3, no. May, 2012.

[31] D. Yoon, Y.-W. Son, and H. Cheong, “Negative Thermal Expansion Coefficient of Graphene Measured by Raman Spectroscopy,” *Nano Lett.*, vol. 11, pp. 3227–3231, 2011.

[32] S. Vantasin *et al.*, “Tip-Enhanced Raman Scattering of the Local Nanostructure of Epitaxial Graphene Grown on 4H-SiC $(000\bar{1})$,” *J. Phys. Chem. C*, vol. 118, no. 44, pp. 25809–25815, Nov. 2014.

[33] J. H. Kang *et al.*, “Strain Relaxation of Graphene Layers by Cu Surface Roughening,” *Nano Lett.*, vol. 16, no. 10, pp. 5993–5998, Oct. 2016.

[34] M. V. Balois-Oguchi *et al.*, “Probing Strain and Doping along a Graphene Wrinkle Using Tip-Enhanced Raman Spectroscopy,” *J. Phys. Chem. C*, vol. 127, no. 12, pp. 5982–5990, Mar. 2023.

[35] C. D. Mendoza, N. S. Figueroa, M. E. H. Maia da Costa, and F. L. Freire, “CVD graphene/Ge interface: morphological and electronic characterization of ripples,” *Sci. Rep.*, vol. 9, no. 1, pp. 1–7, 2019.

[36] S. Goniszewski, M. Adabi, O. Shaforost, S. M. Hanham, L. Hao, and N. Klein, “Correlation of p-doping in CVD Graphene with Substrate Surface Charges,” *Sci. Rep.*, vol. 6, no. March, pp. 1–9, 2016.

[37] K. C. Kwon, K. S. Choi, and S. Y. Kim, “Increased work function in few-layer graphene sheets via metal chloride Doping,” *Adv. Funct. Mater.*, vol. 22, no. 22, pp. 4724–4731, 2012.

[38] Y. Song, W. Fang, A. L. Hsu, and J. Kong, “Iron (III) Chloride doping of CVD graphene,”

*Nanotechnology*, vol. 25, no. 39, 2014.

[39] G. S. Weng, J. L. Luo, and D. G. Ivey, “Galvanic corrosion behavior of GaAs in acid solutions,” *J. Vac. Sci. Technol. A Vacuum, Surfaces, Film.*, vol. 20, no. 3, pp. 1015–1022, 2002.

[40] J. Moore, H. Hendriks, and a Morales, “Characterization and Control of Galvanic Corrosion During GaAs Wafer Photoresist Processing,” *2003 Int. Conf. Compd. Semicond. Manuf.*, no. 831, 2003.

[41] F. Zhou, Z. Li, G. J. Shenoy, L. Li, and H. Liu, “Enhanced room-temperature corrosion of copper in the presence of graphene,” *ACS Nano*, vol. 7, no. 8, pp. 6939–6947, 2013.

[42] L. Liu, K. Q. Peng, Y. Hu, X. L. Wu, and S. T. Lee, “Fabrication of silicon nanowire arrays by macroscopic galvanic cell-driven metal catalyzed electroless etching in aerated hf solution,” *Adv. Mater.*, vol. 26, no. 9, pp. 1410–1413, 2014.

[43] Y. Huang, J. Luo, and D. G. Ivey, “Comparative study of GaAs corrosion in H2SO4 and NH3·H2O solutions by electrochemical methods and surface analysis,” *Mater. Chem. Phys.*, vol. 93, no. 2–3, pp. 429–442, 2005.

[44] M. C. Biesinger, B. P. Payne, L. W. M. Lau, A. Gerson, and R. S. C. Smart, “X-ray photoelectron spectroscopic chemical state Quantification of mixed nickel metal, oxide and hydroxide systems,” *Surf. Interface Anal.*, vol. 41, no. 4, pp. 324–332, 2009.

[45] M. C. Biesinger, B. P. Payne, A. P. Grosvenor, L. W. M. Lau, A. R. Gerson, and R. S. C. Smart, “Resolving surface chemical states in XPS analysis of first row transition metals, oxides and hydroxides: Cr, Mn, Fe, Co and Ni,” *Appl. Surf. Sci.*, vol. 257, no. 7, pp. 2717–2730, 2011.

[46] O. Desplats *et al.*, “On the use of a O 2 :SF 6 plasma treatment on GaAs processed surfaces for molecular beam epitaxial regrowth,” *Appl. Surf. Sci.*, vol. 255, no. 6, pp. 3897–3901, 2009.

[47] H. Shinotsuka, S. Tanuma, C. J. Powell, and D. R. Penn, “Calculations of electron inelastic mean free paths. XII. Data for 42 inorganic compounds over the 50 eV to 200 keV range with the full Penn algorithm,” *Surf. Interface Anal.*, vol. 51, no. 4, pp. 427–457, Apr. 2019.

[48] A. Jablonski and C. J. Powell, “Effective Attenuation Lengths for Different Quantitative Applications of X-ray Photoelectron Spectroscopy,” *J. Phys. Chem. Ref. Data*, vol. 49, no. 3, p. 033102, Sep. 2020.

[49] Z. Liu, Y. Sun, F. Machuca, P. Pianetta, W. E. Spicer, and R. F. W. Pease, “Preparation of clean GaAs(100) studied by synchrotron radiation photoemission,” *J. Vac. Sci. Technol. A Vacuum, Surfaces, Film.*, vol. 21, no. 1, pp. 212–218, 2003.

[50] R. M. Jacobberger, M. J. Dodd, M. Zamiri, A. J. Way, M. S. Arnold, and M. G. Lagally, “Passivation of Germanium by Graphene for Stable Graphene/Germanium Heterostructure Devices,” *ACS Appl. Nano Mater.*, vol. 2, no. 7, pp. 4313–4322, 2019.

[51] J. C. Bourgoin, H. J. von Bardeleben, and D. Stiévenard, “Native defects in gallium arsenide,” *J. Appl. Phys.*, vol. 64, no. 9,. 65–92, 1988.

[52] M. Rebaud, M.-C. Roure, V. Loup, P. Rodriguez, E. Martinez, and P. Besson, “Chemical Treatments for Native Oxides Removal of GaAs Wafers,” *ECS Trans.*, vol. 69, no. 8, pp. 243–250, Sep. 2015.